SOLUTION MINING RESEARCH INSTITUTE
679 Plank Road
Clifton Park, NY 12065, USA

Telephone: +1 518-579-6587
www.solutionmining.org

Technical
Conference
Paper

1965 – 2025

Experimental Assessment of Effective Tensile Strength of Rock Salt and Infiltration Fracture Behavior in Salt Caverns during Gas Operation

Lukas Baumgärtel, Leibniz University Hannover,
Institute of Geotechnical Engineering, Department of
Underground Construction, Hannover, Germany

SMRI Fall 2025 Technical Conference
29-30 September 2025
Wichita, Kansas, United States

Solution Mining Research Institute Fall 2025 Technical Conference

Wichita, Kansas, United States 29-30 September 2025

EXPERIMENTAL ASSESSMENT OF EFFECTIVE TENSILE STRENGTH OF ROCK SALT AND INFILTRATION FRACTURE BEHAVIOR IN SALT CAVERNS DURING GAS OPERATION

Lukas Baumgärtel

Leibniz University Hannover, Institute of Geotechnical Engineering, Department of Underground Construction, Hannover, Germany

Abstract

The geomechanical design of a gas storage cavern requires the determination of the maximum and minimum internal pressures, as well as the injection and withdrawal rates. These parameters are essential for ensuring geomechanical stability and operational safety. During gas withdrawal, the surrounding rock cools due to gas pressure reduction and gas temperature decrease, leading to thermally induced stress reduction in the rock mass. This can temporarily lead to effective tensile stresses on the cavern wall, which can cause infiltration fractures if the existing gas pressure exceeds the smallest compressive stress component plus the effective tensile strength of the rock salt.

To evaluate the effective tensile strength of rock salt, a laboratory program was developed to evaluate the rock salt behaviour under effective tensile stresses. Therefore, a series of specifically designed mechanical extension experiments under gas pressure and different boundary conditions (variation of the test temperature, the initial pressure and the pressure rate on test specimens from different locations) were carried out in the laboratory to simulate the stress conditions occurring in a gas storage cavern during the gas withdrawal phase.

A numerical sensitivity study then integrated the experimental results and investigated the influence on the infiltration fracture length and its distribution using the infiltration fracture approach for a total of three experimentally selected effective tensile strengths and five defined fracture line distances. The infiltration fracture approach is an engineering approach for evaluating the effective tensile stresses on the cavern wall that occur mainly during the gas withdrawal phase.

The experimental results showed that a pressure difference between higher gas pressure and minimal pressure component from 0.99 MPa (143.59 psi) to 4.87 MPa (706.33 psi) was required before macroscopically visible fractures appear. The magnitude of the pressure difference depends in particular on the location, which corresponds to different salt characteristics and textures.

The results of the numerical sensitivity analysis show that the decisive infiltration fracture length should be determined from the mean value of the infiltration fracture length of the modelled fracture lines. This applies to a small rock area (here with 5 defined fracture lines) when a defined fracture line distance is considered, at which the individual fracture lines have a negligible influence on each other (here greater than 1 m), in order to describe the general infiltration fracture behaviour at the cavern wall. Taking different values for the effective tensile strength into account has no significant influence on the determined infiltration fracture length for the selected seasonal load case scenario and the generic cavern in a salt dome.

Key words: Underground gas storage, Infiltration fractures, Effective tensile strength, Effective tensile stress, Rock salt, Salt caverns

Introduction

The geomechanical design of a gas storage cavern is an important part of the planning and construction of a storage cavern in rock salt. It must be demonstrated that the cavern in the rock salt formation remains stable and safe to operate under defined operating conditions, and that the rock mass is tight against the storage medium. In particular, the geomechanical evaluation of the salt caverns must demonstrate that they form no or very small dilatant zones and no or very small effective and absolute tensile stress zones in the rock around the cavern. In order to estimate surface subsidence, the convergence and convergence rate of the rock could also be assessed based on the creep behaviour of the rock salt [1], [2].

The criteria for geomechanical safety are verified for three specified operating parameters: 1. The maximum permissible internal pressure during operation, 2. the minimum gas pressure to be maintained, and 3. the maximum injection and withdrawal rate of the stored gas.

During gas withdrawal from the storage cavern, the surrounding rock cools down due to the thermodynamic behaviour of natural gas, which cools when pressure is released. The cooling of the cavity causes thermally induced stress changes in the rock, which can lead to effective tensile stresses and local fractures if the prevailing gas pressure in the cavern is higher than the sum of the effective tensile strength and the smallest compressive rock stress component [3].

The presence of thermally-induced fractures was substantiated through field observations [4], wherein a temperature gradient of -20 K was recorded, and in field studies [5] under specified boundary conditions exhibiting elevated temperature gradients.

It is therefore necessary to consider the resulting temperature gradients and thermally induced strains that arise due to the above-mentioned thermodynamic behaviour of the gas and its effects on the surrounding cavern wall. It has been demonstrated that not taking into account thermal effects within the cavern leads to stress conditions in the rock that cannot reflect and underestimate the thermally induced stresses that occur [6]. This is particularly important in connection with the geomechanical assessment of the rock during cavern operation.

To provide a more detailed description of the behaviour of rock salt under high pressure and simultaneous cooling, as prevails in gas storage caverns during the gas withdrawal phase, its further investigation within this area has to be conducted. The field investigations mentioned [4], [5] were carried out under atmospheric pressure conditions.

Initial experimental investigations at this thermally-induced pressure conditions in the laboratory at the Institute of Geotechnical Engineering at Leibniz University Hannover showed that the rock salt hollow test specimen ruptures as soon as a certain effective tensile stress value is reached under applied triaxial pressures and internal gas pressure [7], [8].

As part of this work, an extensive laboratory programme was carried out on rock salt from four different locations. The objective of the programme was to investigate the material behaviour under effective tensile stresses, such as those expected to be thermally induced in the gas withdrawal phase of a cavern, by means of mechanical extension tests. The effective tensile strength in relation to the external triaxial load, test temperature and pressure reduction rate was tested for this purpose.

The effects of the results obtained in the laboratory were then examined numerically using a generic cavern model and operation. For this purpose, horizontal fracture lines were implemented in a continuum model and the behaviour is examined for different effective tensile strengths and vertical fracture line distances.

Finally, recommendations for the application of the infiltration fracture criterion were derived based on the laboratory tests conducted and the numerical investigations.

Experimental Investigation

The aim of the experimental investigations was to determine the effective tensile strength of rock salt from various locations under different boundary conditions in order to determine the level and dependencies of the effective tensile strength and consequently to better describe the infiltration fracture behaviour in the vicinity of salt caverns.

In total, rock salt was sampled from four different locations, which exhibited different grain compositions and degrees of impurities (see Figure 1). Locations X and Y originate from salt mines in Germany (Location X) and the USA (Avery Island [9], Location Y). The test specimens shown here from locations Z and B originate from cavern wells in Germany.

The test specimens from location X have relatively large grains with predominantly good sorting. The grain boundaries are clearly visible under transmitted light. The grain sizes from location Y are comparatively small and the sorting is also homogeneous. The test specimens from the cavern boreholes (Locations Z and B) show poor grain sorting and visibly increased levels of impurities.

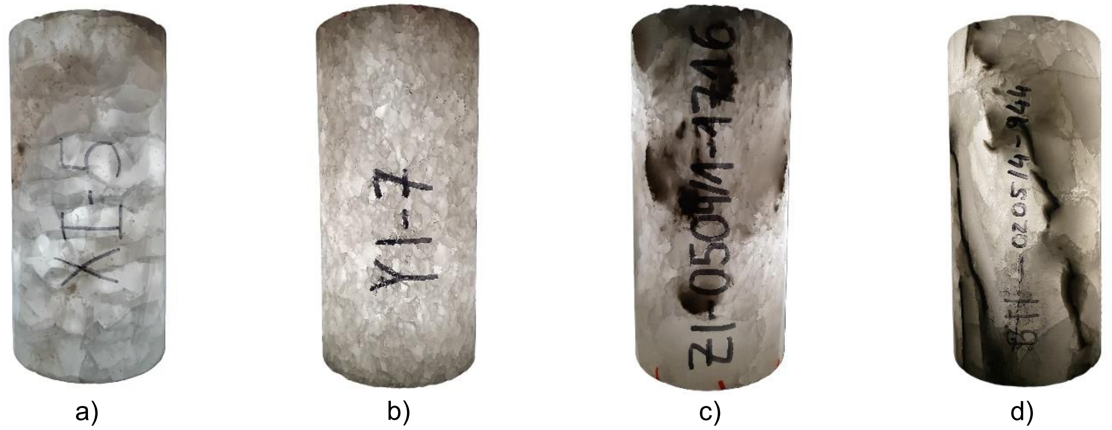

a) b) c) d)

Figure 1: Test specimens prepared from locations (a) X, (b) Y, (c) Z and (d) B under transmitted light.

A test setup was designed that made it possible to generate effective tensile stresses leading to material failure under external triaxial loading and internal gas pressure in a hollow cylinder of rock salt.

The cylindrical hollow test specimens were turned to an outer diameter of 90 mm (3.54 in) and a height of 180 mm (7.08 in) and then drilled through to an inner diameter of 30 mm (1.18 in).

It was also necessary to bond the test specimens at the top and bottom using a system of steel plugs and steel plates and to fit them with packers in order to generate the effective tensile stresses mentioned above (see Figure 2a). The test gas (nitrogen was used here) was fed into the hollow test specimen through the gas screw, which is drilled axially in the centre. The test specimen was clamped to the pressure plates using the specified screws.

The experiment was divided into three steps, which are explained below and shown schematically in Figure 2b.

1. **Loading Phase:** The three pressure components (axial pressure p_{ax}, circumferential pressure p_m and gas pressure p_i) were first brought to an initial pressure level, which is reached at the end of the loading phase. The gas pressure was increased slightly in a staggered manner to prevent any previous infiltration fracture processes. The initial gas pressure is approx. 0.5 MPa (72.5 psi) below the external initial pressures.
2. **Standing Phase:** The reached pressure level was then maintained for 2 hours to bring the pressure-induced temperature rise within the triaxial cell back to the planned test temperature. This pressure level also serves as the starting point for the unloading phase.

3. **Unloading Phase:** After a two-hour standing phase, the axial pressure p_{ax} was reduced while maintaining the circumferential pressure p_m and gas pressure p_i until the rock salt test specimen failed, which was verified by a horizontal fracture of the test specimen after removal.

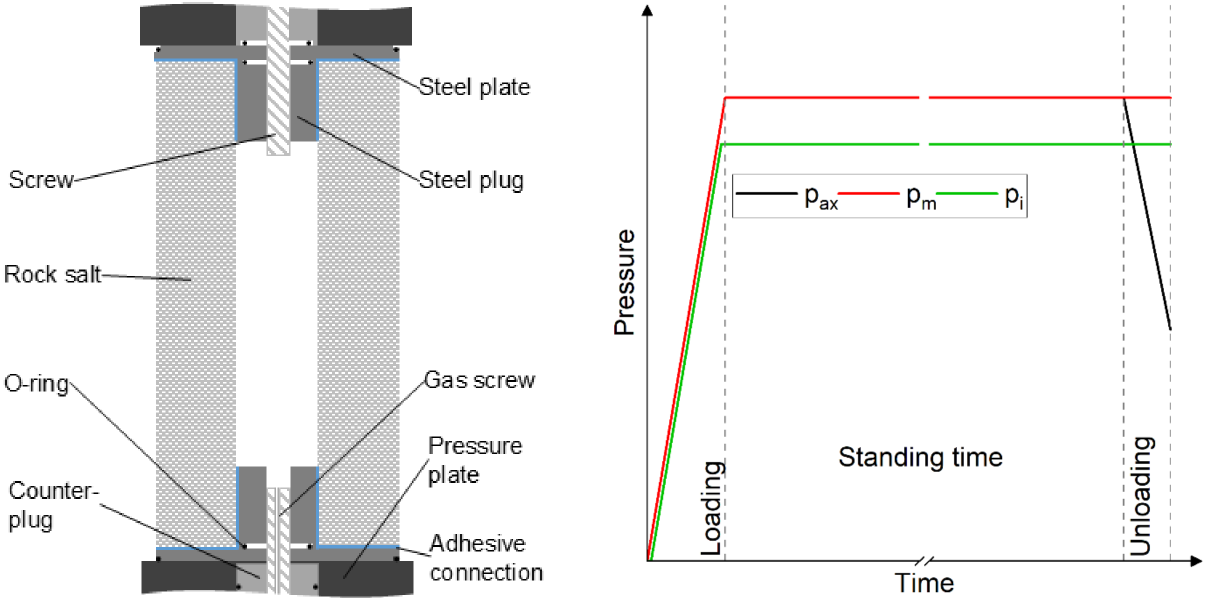

a) b)

Figure 2: (a) Test setup and (b) schematic test procedure.

The axial pressure component was chosen for reduction because the numerical results for the operation of a gas storage cavern show that the vertical stress component in particular decreases at the cavity edge during gas withdrawal (due to cooling of the gas) and has lower compressive stress values than the prevailing gas pressure [3] (see also Figure 7). This results in effective tensile stresses at the cavity of the cavern.

For the test, the static test temperature (303.15 K and 323.15 K), the initial pressure level (8 MPa (1160.3 psi), 13 MPa (1885.5 psi) and 18 MPa (2610.7 psi)) and the following different axial pressure unloading rates were investigated for the locations shown above:

- -0.001 MPa/min (-0.145 psi/min),
- -0.01 MPa/min (-.1.45 psi/min),
- -0.02 MPa/min (-2.9 psi/min),
- -0.05 MPa/min (-7.25 psi/min),
- -0.1 MPa/min (-14.5 psi/min),
- and -1.0 MPa/min (-145 psi/min).

In particular, the sensitivities of the selected test temperature and initial pressure levels were investigated at an unloading rate of -1.0 MPa/min (-145 psi/min). A sensitivity analysis of the different pressure unloading rates was only carried out with a small number of successful tests.

During the test, the axial and circumferential displacements, the three pressure components, and acoustic emissions, at a frequency of 50 Hz using a sensor installed in the lower pressure plate, were recorded.

First, the findings between differently selected pressure reduction rates are shown (see Figure 3 and Figure 4). The selected illustrations also enable the basic test procedure in the unloading phase of the test to be understood. The initial pressures (p_{ax} = p_m = 8.0 MPa / 1160.3 psi, p_i = 7.5 MPa / 1087.8 psi) and test temperatures (303.15 K) were the same for both tests shown here.

Figure 3 shows the three pressure components over time in the unloading phase of the respective exemplary tests. In the test with a faster axial pressure reduction rate (see Figure 3a), a pressure difference between the axial and gas pressure of 2.01 MPa (291.53 psi) resulted in a significant increase in the axial pressure and failure of the rock salt specimen (see photo in Figure 4), which was also accompanied by a strong axial displacement change in the negative direction (extension). Due to the selected rate, the unloading time was just under 180 seconds.

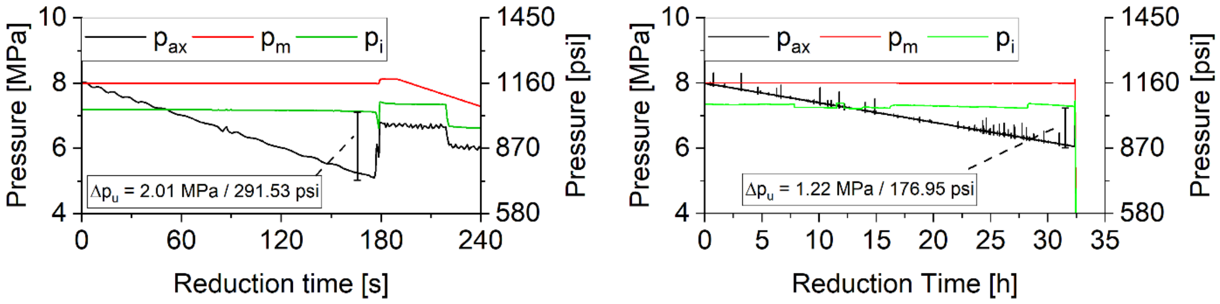

a)

b)

Figure 3: Plot of the three pressure components for the unloading phases with different pressure reduction rates: (a) -1.0 MPa/min (-145 psi/min) (b) -0.001 MPa/min (-0.145 psi/min).

The mechanical extension test with an axial pressure reduction rate of -0.001 MPa/min (-0.145 psi/min) took correspondingly longer and the test specimen ruptured at a pressure difference Δp of 1.22 MPa (176.95 psi) between axial and gas pressure after more than 30 hours of unloading time (see Figure 3b). During the unloading phase, selective increases in the pressure level could be observed in the axial pressure, which is related to the pressure control of the axial load and the very low rate, which is challenging in controlling. The basic result of the experiment is not visibly affected by this.

In the next step, the recorded acoustic emissions are plotted as a function of the pressure difference Δp in the unloading phase (see Figure 4). In addition, the axial strains ε_{ax} are plotted against the pressure difference Δp. The axial strains ε_{ax} are set to 0 at the beginning of the unloading phase. Figure 4a displays these for the aforementioned test with a pressure reduction rate of -1.0 MPa/min (-145 psi/min), and in Figure 4b for the slower rate in comparison. The axial strain value at the highest pressure difference value indicates the point at which the test specimen ruptured. The subsequent further extension (decreasing axial strain) built up immediately after rupture over a brief period of time.

A comparison of the acoustic emissions occurring across the pressure difference Δp for different axial pressure reduction rates shows that, due to the faster unloading at a higher axial pressure reduction rate, visible acoustic emissions indicating infiltration and microcrack processes in the rock salt prior to rupture in this experiment only occur in the effective tensile stress range (see Figure 4a), i.e. when the gas pressure p_i is greater than the axial pressure p_{ax}. For the much slower rate, such processes are already visible at effective compressive stresses, but the number of acoustic emissions measured per pressure interval remains at a lower level (see Figure 4b). It can therefore be assumed that, at a slower rate, the infiltration process is spread over a larger pressure difference range, which is also associated with the long test duration. This also results in longer exposure to effective tensile stresses, which could lead to a reduction in the pressure difference Δp, causing the test specimen to rupture under effective tensile stresses in this load regime. The recorded axial strains ε_{ax} are also higher for a faster pressure change rate in terms of magnitude, depending on the pressure difference Δp at the time of rupture (highest value of the pressure difference). Here too, the less pronounced infiltration processes that occur in the unloading phase do not play as significant a role as they would at a very slow rate due to the comparatively rapid unloading. This results in greater axial extension before the test specimen ruptures, i.e. before the infiltration fracture occurs.

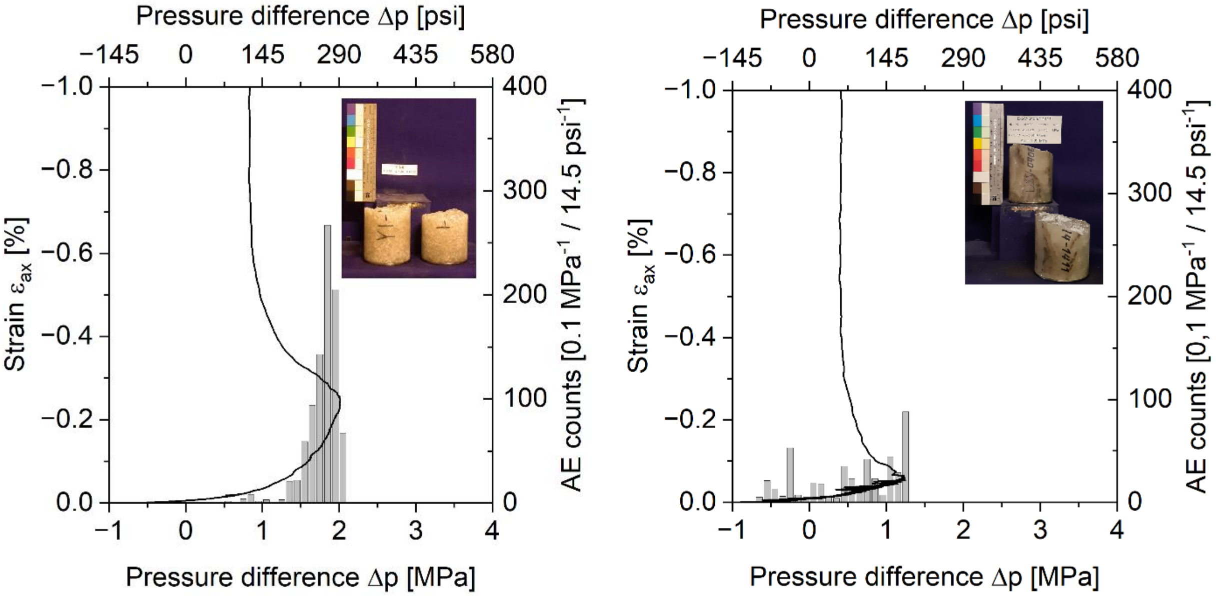

a) b)

Figure 4: AE-counts and axial strain ε_{ax} over pressure difference Δp for two different pressure reduction rates: (a) -1.0 MPa/min (-145 psi/min) (b) -0.001 MPa/min (-0.145 psi/min) and pictures of the test specimen after the experiment.

The pressure differences Δp_u achieved, which can be declared as the effective tensile strength β_{eff}^{T} of the material and which lie between 0.99 MPa (143.59 psi) and 4.87 MPa (706.33 psi) for all tests carried out, show a non-significant linear dependence on the selected initial pressure level or the selected test temperature. However, a significant linear dependence between the prevailing gas pressure $p_{i,u}$ and the minimum pressure $p_{min,u}$ applied, which in this case is the axial pressure $p_{ax,u}$, can be observed (see Figure 5). The aforementioned increased degree of impurity and poor grain sorting at location Z leads to a greater variation in the pressure differences at the respective pressure levels tested. This is not apparent to this extent at locations X and Y. In both cases, the grain structure is better sorted and there is little to no impurity. The variation is also evident in the standard error of the linear approximation functions of the locations. This is comparatively high at location Z with ± 0,24 MPa (± 34.81 psi). The fit functions shown in Figure 5 are listed below:

- Loc. X (black): $p_{i,u} = p_{ax,u} + 1.55$ MPa (224.81 psi) (± 0,09 MPa (± 13.05 psi)), R² = 0,996
- Loc. Y (red): $p_{i,u} = p_{ax,u} + 2.45$ MPa (355.34 psi) (± 0,11 MPa (± 15.95 psi)), R² = 0,992
- Loc. Z (green): $p_{i,u} = p_{ax,u} + 2.73$ MPa (395.95 psi) (± 0,24 MPa (± 34.81 psi)), R² = 0,961

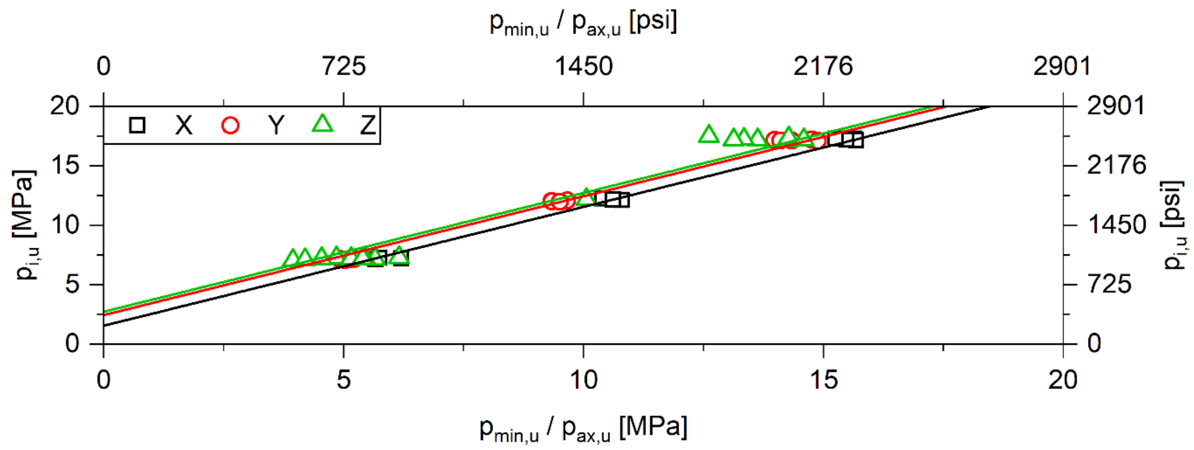

Figure 5: Gas pressure as a function of the minimum pressure (here: axial pressure) at the moment of rupture of the test specimen.

The intersection with the y-axis represents an indicator of the average effective tensile strength β^T_{eff} of the test specimens tested per location, with the highest value being determined for location Z and the lowest value for location X. The slope of the linear approximation shown here is 1 for all locations, and the statistical coefficient of determination R^2 is above 95% in all cases. The results achieved for the pressure difference Δp_u are within the ranges also achieved in similar tests with rock salt in [10], [11], [12], albeit with a different test setup, test procedure and different objectives of the investigation. For a detailed comparison of the test results, see [13].

The magnitude of the pressure difference Δp_u that leads to rupture of the test specimen, depending on different pressure change rates, was demonstrated for one test per pressure level (see Figure 6). The transfer to general material behaviour is therefore only possible to a limited extent. It should be noted that the test is more demanding at low axial pressure reduction rates, as the test specimen and the adhesive bonds between the test specimen and the steel components are subjected to effective tensile stresses over a long period of time. As soon as there are leaks in the system, the test is terminated without visible material failure.

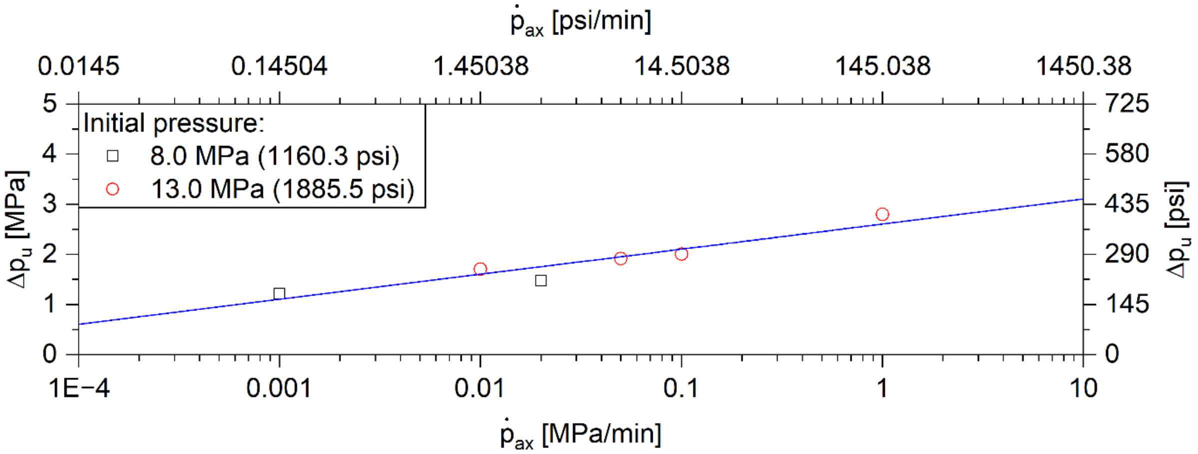

Figure 6: Pressure difference as a function of the axial pressure reduction rate (one test per axial reduction rate).

Figure 6 shows an increase in the linear dependence with increasing axial pressure reduction rate. The corresponding fit function is not shown here, as only one test was performed for axial pressure reduction rates of less than 1 MPa/min (14.5 psi/min). In order to demonstrate a valid dependence of the pressure change rate on the pressure difference, it is recommended to carry out a higher number of successful experiments per pressure stage with test specimens with a homogeneous salt structure (e.g., from locations X or Y), which lead to negligible variations in the results.

In summary, the experiments conducted have shown that material failure occurs as soon as an effective tensile stress value is exceeded. The magnitude depends in particular on the salt structure, which was described visually in this work. A dependence of the gas pressure $p_{i,u}$ leading to the rupture of the test specimen depends solely on the minimum pressure $p_{min,u}$ (here: $p_{ax,u}$) applied.

The experimentally determined value range for effective tensile strength β_{eff}^{T} will be integrated into numerical investigations in the next step in order to examine the effects of existing effective tensile strength on the formation of infiltration fractures during the operation of a gas storage cavern.

Numerical Implementation

The numerical investigations focus on thermally induced infiltration fracture at the cavern wall during the operation of gas storage caverns. Particularly during the gas withdrawal phase, thermodynamic cooling of the gas leads to temperature reductions at the cavern wall, which in turn causes thermally induced changes in rock stress. Figure 7 shows the stress and temperature curve over the calculated cavern operation. Cavern operation begins after a pre-operation period of 730 days. The stress component σ_{xx} at the point under consideration approximately represents the radial stress, the stress component σ_{yy} represents the circumferential stress, and the stress component σ_{zz} represents the vertical stress. The radial component acts against the applied gas pressure and thus follows its course. It can be seen that when the gas pressure p_i is reduced, i.e., when gas is withdrawn, the temperature in the cavern drops and the vertical stress at the edge of the cavity enters a range that has lower compressive stress than the applied gas pressure p_i.

The experimental results showed that infiltration and subsequent infiltration fracturing occur as soon as a certain effective tensile stress value is exceeded.

The numerical model considers a quarter model of the cavern (see Figure 7) in the salt dome and assumes axial symmetry. The last cemented casing shoe (LCCS) is located at a depth of 1,000 m (3280.8 ft) and the cavern has a diameter of 70 m (229.7 ft). The deepest point of the cavern is at 1,400 m (4593.1 ft). The cavern neck has a modelled length of 30 m (98.4 ft). The cavern roof and cavern sump are modelled elliptically.

The salt top is assumed to be at a depth of 500 m (1640.4 ft). The rock salt material is modelled with stress, temperature and time dependent elastic-viscous deformation behaviour using the Lubby2 [14] material law. The selected parameters (see in [13]) address the lower bandwidth for rock salt in northern Germany. The calculation with Itasca Flac3D [15] was then performed in a thermo-mechanically coupled mode, with the thermodynamic behaviour of the stored natural gas being calculated using KavPool [16].

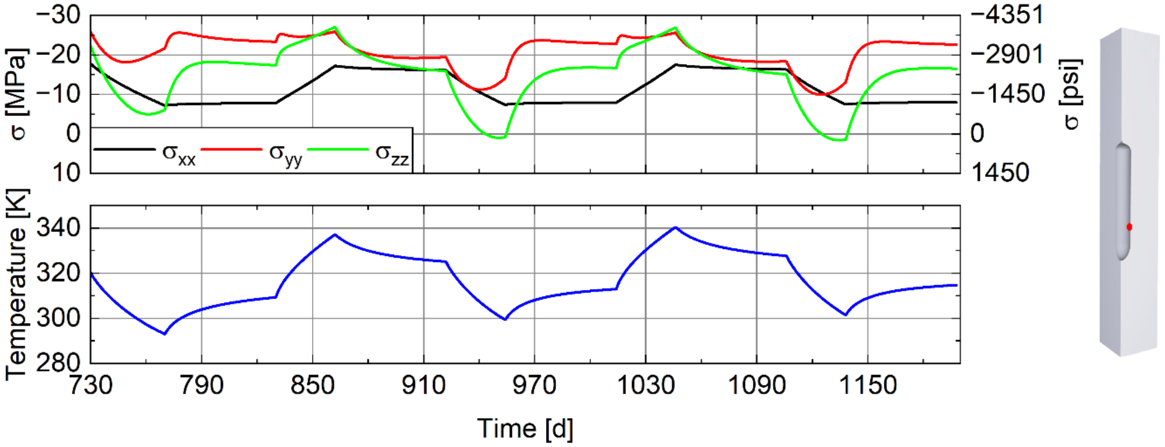

Figure 7: Stress and temperature curve over time at the edge of the cavern cavity.

Based on the infiltration fracture criterion, which is also used in [17], [3], among other places, the influence of an experiment-based effective tensile strength was investigated. Another subject of investigation was the distance between the pre-modelled defined possible fracture lines along which infiltration fractures can propagate in a radial direction. For this purpose, a total of five defined fracture lines was modelled, and five different vertical distances a_R were selected, which are shown in Figure 8. The vertical distances a_R between the respective defined fracture lines are 0.2 m (7.87 in), 0.5 m (19.69 in), 1.0 m (39.37 in), 1.5 m (59.06 in) and 2 m (78.74 in).

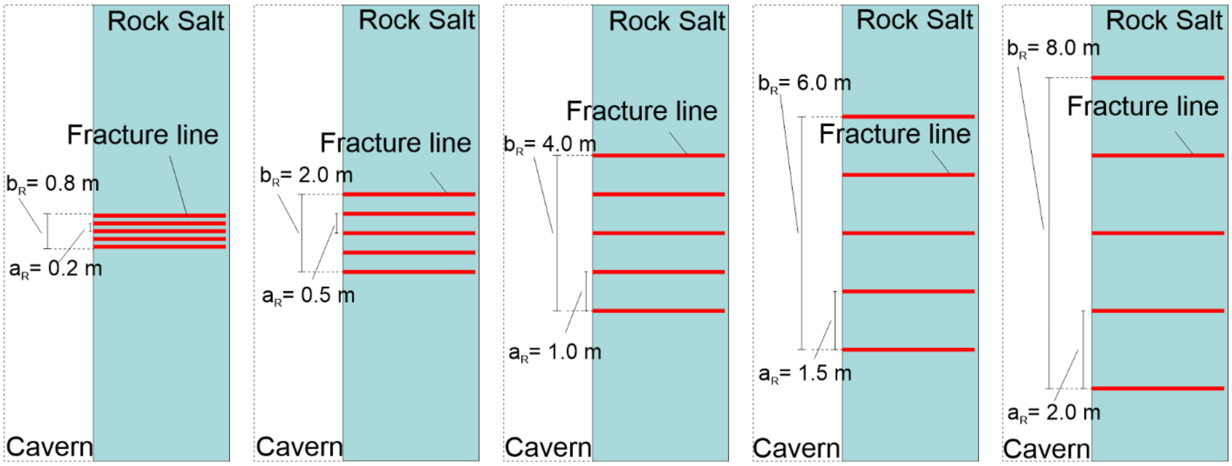

a) a_R = 0.2 m b) a_R = 0.5 m c) a_R = 1.0 m d) a_R = 1.5 m e) a_R = 2.0 m

Figure 8: Schematic representation of the five defined fracture lines per variation model with different vertical distances a_R. b_R indicates the vertical distance between the top and bottom defined fracture lines.

The infiltration fracture behaviour is examined via simulated operation at the most critical point on the edge of the cylindrical cavity, which is located in the upper third of the cavern [13]. In this instance, too, the vertical stress decreases significantly during the gas withdrawal phase, and effective tensile stresses arise. This leads to material failure when the gas pressure p_i is greater than or equal to the sum of the amount of the vertical stress σ_{zz} and the effective tensile strength β_{eff}^{T}. The infiltration fracture criterion is only applicable in the compressive stress range.

$$p_i \geq |\sigma_{zz}| + \beta_{eff}^{T} \tag{1}$$

The condition is checked for the adjacent zones in the defined fracture lines and, if fulfilled, the outer zone in the defined fracture lines is deleted. The gas pressure is then also applied as a load to the fractured area that has been opened.

In the numerical study, effective tensile strengths β_{eff}^{T} of 1.0 MPa (145 psi) and 2 MPa (290 psi) were investigated, which represents the lower bandwidth of the values determined in the experimental investigations. Furthermore, it was investigated what the behaviour would be if there were no effective tensile strength. As a result, a total of 15 different models were calculated for the sensitivity analysis of the specified effective tensile strength β_{eff}^{T} and the defined vertical fracture line distances a_R.

The infiltration fractures propagate in particular during the first calculated gas withdrawal phase; whereby effective tensile stresses arise for the first time in the calculation model between the gas pressure and the vertical rock stresses at the point under consideration in the upper third of the cavern cavity edge. In the subsequent pressure reduction phases (a total of three phases were calculated), the infiltration fractures continue to propagate along the respective defined fracture lines, particularly if a higher effective tensile stress is achieved than in the previous cycles.

The results at the end of the calculation model (see Figure 9) show that the infiltration fracture lengths differ only slightly from each other at a vertical distance of the defined fracture lines between 2 m (78.74 in) and 1 m (39.37 in) and for all effective tensile strengths β_{eff}^{T} investigated. This applies to the comparison between the model variations and to the individual fracture lines 1 to 5 in the respective models. In these model variations, the relative infiltration fracture length is greater than 80% for all infiltration fractures when the longest infiltration fracture formed is used as the reference value. The average calculated infiltration fracture length for these model variations is between 2.0 m (78.74 in) and 2.3 m (90.55 in). It should be noted that a zone width of 0.25 m (9.84 in) was selected in the radial direction in the fracture zones. The fracture progression thus took place in this increment.

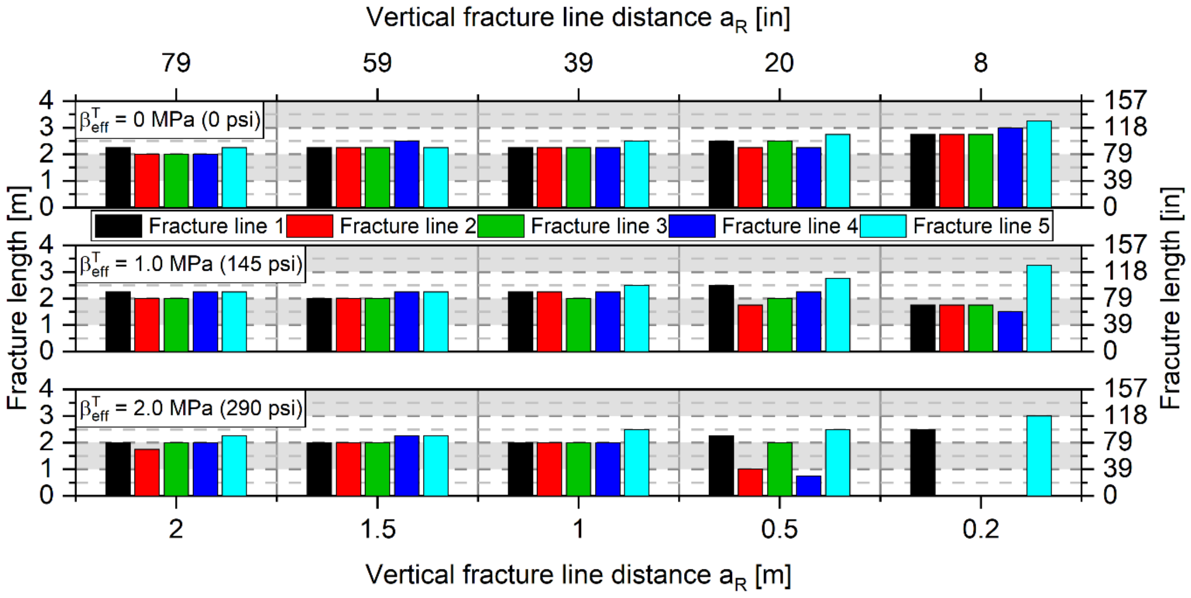

Figure 9: Infiltration fracture lengths determined after calculating the operating load case shown above for the individual fracture lines and the various model variations (inch values rounded to whole numbers).

It is also apparent that the infiltration fracture lines are at a similar level even at defined fracture distances of less than 1 m when the material has no effective tensile strength. Fracture line 5, which is the furthest down, shows a slightly longer infiltration fracture length. This can be explained, among other things, by the edge location of the fracture, since the rock stresses that occur are mainly dissipated via this defined fracture line and, on the other hand, vertical stresses below the fracture area remain at a similar level over a larger area in the depth direction.

Dependencies for the vertical fracture line distances and the assumed effective tensile strength β_{eff}^{T} of the material can be seen in particular for a distance of 0.5 m (19.69 in) or 0.2 m (7.87 in) and an effective tensile strength of 2 MPa (290 psi). In the model with the smallest vertical fracture distance, infiltration fractures only form on the outer fracture lines, which are of comparable length. No effective tensile stresses greater than the assumed effective tensile strength β_{eff}^{T} of 2 MPa (290 psi) arise between these two infiltration fractures. At the same time, however, this also means that the selected model variation does not allow conclusions to be drawn about the basic infiltration fracture behaviour across the entire cavity edge, as the number of infiltration fracture lines formed with such a small defined vertical fracture line distance is not sufficient for a general assessment.

The analysis and evaluation of the numerical results obtained from the fifteen model variations calculated to evaluate the sensitivity of the effective tensile strength and the vertically defined fracture line distance allow the following conclusions to be drawn:

1. The infiltration fracture length should be evaluated using the mean value at fracture line distances that has a negligible influence on the infiltration fracture distribution (here between 1.0 m (39.37 in) and 2.0 m (78.74 in)) in order to adequately estimate the overall infiltration fracture behaviour with a small fracture area under consideration.
2. Taking into account the first point mentioned, the necessity of considering an effective tensile strength cannot be derived from the results obtained.

Summary

Thermally induced infiltration fractures occur in the cavity edge area of gas storage caverns in rock salt when the internal pressure exceeds the sum of the smallest compressive stress and the effective tensile strength of the salt – this occurs in particular during gas withdrawal. These fractures are limited to a narrow radial area near the cavern wall.

To evaluate these effective tensile stresses, a discrete fracture approach was applied within a continuum model using predefined fracture lines. This enabled simulation of infiltration fracture formation in localised areas, which also allowed transfer to the basic behaviour of infiltration fracture formation.

The magnitude of the critical pressure difference Δp_u, which indicates the effective tensile strength β_{eff}^{T} of rock salt, was determined in an extensive laboratory programme using novel mechanical extension tests. It marked the onset of macroscopic failure and was particularly influenced by the salt structure of the different locations tested. Values for the effective tensile strength β_{eff}^{T} between 0.99 MPa (143.59 psi) and 4.87 MPa (706.33 psi) were determined on test specimens from different locations.

The numerical sensitivity analysis with regard to the influence of the selected effective tensile strength β_{eff}^{T} and the defined vertical fracture line distance showed that the decisive infiltration fracture length can be determined from the mean value of the infiltration fracture lengths for a defined vertical fracture line distance, whereby the resulting infiltration fractures do not visibly influence each other (here greater than 1 m (39.37 in)). In this case, the infiltration fracture lengths determined are of comparable length.

When the upper guideline is used, the consideration of an effective tensile strength in the generic model shows only a minor influence on the calculated fracture length. It follows that an intensive determination of the effective tensile strength β_{eff}^{T} based on the generic cavern model calculated here does not appear necessary.

Acknowledgements

I would like to thank SMRI for providing rock salt from Avery Island, which was used in this research work.

In addition, the research project ‘LARISSA’ was funded by the Federal Ministry for Economic Affairs and Energy (BMWE) as part of the 7th Energy Research Programme (FKZ: 03EI3028), which made the work presented here and the achieved results possible.

Finally, I would like to thank my current employer, AtkinsRéalis, for providing me with the time and financial support to present the results of my doctoral thesis at the SMRI conference.

References

[1] B. Brouard, P. Bérest, and M. Karimi-Jafari, “Onset of Tensile Effective Stresses in Gas Storage Caverns,” presented at the SMRI Fall 2007 Technical Meeting, Halifax, Canada, Oct. 2007.

[2] R. Habibi, “An investigation into design concepts, design methods and stability criteria of salt caverns,” *Oil Gas Sci. Technol. – Rev. IFP Energies nouvelles*, vol. 74, p. 14, 2019, doi: 10.2516/ogst/2018066.

[3] D. Zapf, R. B. Rokahr, B. Leuger, and S. Yildirim, “Influence of Infiltration Fractures on the Stress Field in the Vicinity of Gas Storage Caverns in Rock Salt,” presented at the SMRI Spring 2019 Technical Conference, New Orleans, Louisiana, USA, Apr. 2019.

[4] S. Heusermann and R. Eickemeier, “Einfluss der Bewetterungstemperatur auf das mechanische Verhalten des Schachtes 1 im Erkundungsbergwerk Gorleben,” in *Messen in der Geotechnik 2008*, in Mitteilung des Instituts für Grundbau und Bodenmechanik Technische Universität Braunschweig, no. 87. , Braunschweig, Germany, 2008, pp. 145–162.

[5] C. Balland *et al.*, “Acoustic monitoring of a thermo-mechanical test simulating withdrawal in a gas storage salt cavern,” *International Journal of Rock Mechanics and Mining Sciences*, vol. 111, pp. 21–32, Nov. 2018, doi: 10.1016/j.ijrmms.2018.07.023.

[6] K. Staudtmeister and D. Zapf, “Rock Mechanical Design of Gas Storage Caverns for Seasonal Storage and Cyclic Operations,” presented at the SMRI Spring 2010 Technical Conference, Grand Junction, Colorado, USA, Apr. 2010.

[7] R. B. Rokahr, D. Zapf, B. Leuger, and L. Siemann, “Laboruntersuchungen von thermisch-induzierter und gasdruckgetriebener Rissbildung im Salzgestein (La-thi-ga),” Leibniz Universität Hannover, 2021. doi: 10.2314/KXP:1775726282.

[8] B. Leuger, L. Baumgärtel, D. Zapf, and F. Körner, “Laboratory Investigations of Fracture Propagation in Rock Salt in Hollow Test Specimens - LARISSA Research Project,” presented at the SMRI Fall 2023 Technical Conference, San Antonio, Texas, USA, Oct. 2023.

[9] S. A. Buchholz, E. L. Krantz, J. P. Knight, and T. R. Artz, “Retrieval, Storage, and Distribution of Standard Salt Core From Avery Island,” RESPEC, Rapid City, SD, USA, SMRI Research Report RR2019-1, 2019.

[10] P. Kiersten, “Das Hydrofrac-Verhalten von Steinsalz in Abhängigkeit von der Probeneinspannung, der Druckrate, der Flüssigkeitsviskosität und der Standdauer,” Dissertation, Technische Universität Clausthal, Clausthal-Zellerfeld, Germany, 1983.

[11] K. Schlüter, “Das Hydrofrac-Verhalten von Salzgesteinen in Abhängigket von der Salzart, Einspannung und Druckerhöhungsrate,” Dissertation, Technische Universität Clausthal, Clausthal-Zellerfeld, Germany, 1986.

[12] W.-P. Kamlot, “Gebirgsmechanische Bewertung der geologischen Barrierefunktion des Hauptanhydrits in einem Salzbergwerk,” Habilitation, TU Bergakademie Freiberg, Freiberg, Germany, 2009.

[13] L. J. Baumgärtel, “Experimentelle und numerische Untersuchungen zu Infiltrationsrissen bei effektiven Zugspannungen in der Umgebung von Salzkavernen,” Leibniz Universität Hannover, Hannover, Germany, 2025. doi: 10.15488/19183.

[14] D. Zapf, F. Körner, B. Leuger, and L. Baumgärtel, “Modification of the Rock Mechanical Design of Salt Caverns on the Basis of Recent Research,” in *58th U.S. Rock Mechanics/Geomechanics Symposium*, Golden, Colorado, USA: ARMA, Jun. 2024. doi: 10.56952/arma-2024-0145.

[15] Itasca Consulting Group, Inc., *FLAC3D - Fast Lagrangian Analysis of Continua in Three-Dimensions*. (2024). Minneapolis, USA.

[16] ESK GmbH, *KavPool*. (2022). Freiberg, Germany.

[17] S. Yildirim, “Berücksichtigung des mechanischen Schädigungsverhaltens von Salzgestein bei der Berechnung von Infiltrationsrissen im Randbereich von Gasspeicherkavernen,” Dissertation, Leibniz Universität Hannover, Hannover, Germany, 2019.